Comparison of magnetostatic field calculation methods on 2-D square grids as applied to a micromagnetic standard problem

R. D. McMichael, M. J. Donahue, and D. G. Porter
National Institute of Standards and Technology, Gaithersburg, MD 20899

Jason Eicke
Institute for Magnetics Research, George Washington University, Washington, DC 20052
(January 29, 1999)

Magnetization reversal modes and coercivities were calculated for a magnetic particle with thickness : width : length aspect ratios 0.1 : 1 : 5 as a function of the reduced particle width d/l_{ex}, where d is the particle width and l_{ex} is the intrinsic magnetostatic exchange length. With only exchange energy and magnetostatic energy included, the particle corresponds to μMAG standard problem #2. The problem is modeled with 2D grids of 3D spins, and the results are compared for two methods of calculating magnetostatic energies, the "constant magnetization" method and the "constant charge" method.

For both magnetostatic computational methods, the coercivity decreases from $H_c/M_s = 0.06 \pm 0.003$ to 0.014 ± 0.003 over the range $3 < d/l_{\rm ex} < 80$, where the uncertainties reflect the field step size. Also over this interval, as $d/l_{\rm ex}$ increases, the magnetization exhibits three modes of reversal: nearly uniform rotation, transverse switching of end domains followed by propagation of head-to-head domain walls from the ends to the center of the particle, and nucleation and propagation of vortices accompanied by more complex domain structures.

I. INTRODUCTION

The particle defined by μMAG standard problem #2 is rectangular, with thickness : width : length aspect ratios 0.1 : 1 : 5. Only the exchange energy, characterized by the stiffness constant, A, and the magnetostatic energy, characterized by the spontaneous magnetization, M_s, are considered. Fields are applied along the [1,1,1] axis[1]. Calculations were done as a function of the reduced particle width d/l_{ex}, where d is the particle width and $l_{ex} = (2A/\mu_0 M_s^2)^{1/2}$ is the intrinsic exchange length.

For computational convenience, we have assumed 1) that the magnetization is uniform across the thickness of the sample, and 2) that it is sufficient to calculate magnetostatic fields in the mid plane of the film. The first assumption is implicit in our use of 2D grids. These assumptions make it possible to separate the computation of the self-magnetostatic field, $\mathbf{H}^{\rm D}$, into in-plane, $\mathbf{H}^{\rm D}_{\mathbf{x,y}}$, and out-of-plane, $H_z^{\rm D}$, components where only M_z contributes to $H_z^{\rm D}$ and only $\mathbf{M}_{x,y}$ contributes to $\mathbf{H}^{\rm D}_{\mathbf{x,y}}$.

Because the calculation of the magnetostatic energy and/or field in micromagnetic simulations is the most time consuming part of the calculation, there has been a great deal of interest in finding optimal computational techniques for magnetostatics. This paper describes magnetization reversal mechanisms and critical fields for μMAG standard problem #2 using two methods of calculating the in-plane components of magnetostatic fields, the constant magnetization method[2], and the constant charge method[3,4].

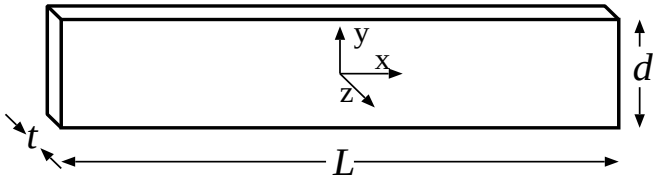

FIG. 1. The geometry of μMAG standard problem #2, a 0.1:1:5 aspect ratio rectangular block of magnetic material with exchange energy, magnetostatic energy and Zeeman energy only.

The magnetization was relaxed according to Landau-Lifshitz damping, $d\mathbf{M}/dt = -\frac{\lambda}{M_s}\mathbf{M} \times (\mathbf{M} \times \mathbf{H})$, where $\mathbf{H}$ includes $\mathbf{H}^D$, the applied field, and the exchange field, computed using an eight-neighbor cosine scheme[5].

For both of the methods for calculating $\mathbf{H}^{\rm D}$ described

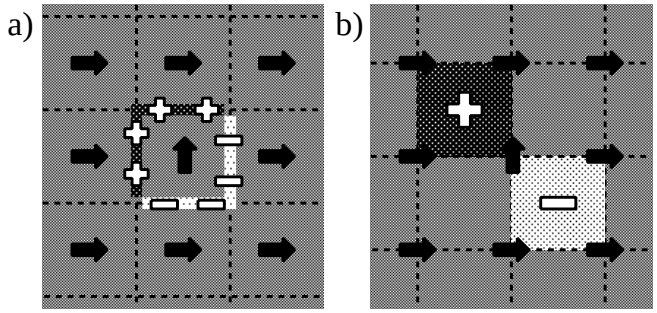

FIG. 2. Illustration of the magnetostatic charge distributions surrounding a single misoriented spin a) in the constant magnetization method and b) in the constant charge method.

below, we use real fast Fourier transform (FFT) techniques to evaluate convolution integrals. To eliminate periodic image charges introduced by the discrete FFT, we embed the region of interest in zero-padded arrays at least twice as large as the sample grid in each dimension.

Also, for both methods of computing $\mathbf{H}^{\mathrm{D}}_{\mathbf{x,y}}$, H^{D}_z is calculated by a constant magnetization method (see below) because the magnetization is assumed to be uniform through the thickness of the sample. The computation of H^{D}_z contributes two real FFT's to the cost of each of the methods of computing $\mathbf{H}^{\mathrm{D}}$.

In the constant magnetization method, $\mathbf{M}$ is assumed to be uniform throughout each grid cell, and discontinuous at the cell boundaries. The Fourier transforms of $\mathbf{M}_x$ and $\mathbf{M}_y$ are multiplied by a kernel which is the Fourier transform of the in-plane demagnetization tensor, computed using an analytic expression[2]. In the final step, in-plane magnetostatic fields are obtained by inverse transforms of the tensor product.

The computational cost of this method of computing $\mathbf{H}^{\mathrm{D}}_{\mathbf{x,y}}$ includes four real FFT's per evaluation.

The constant charge method is described in detail in Refs. 3, 4 for the case where one dimension of the sample is infinite. We have modified the technique for the case of thin films. For the constant charge method it is convenient to assume that spins lie on the corners of a grid as illustrated in Fig. 2b. Each cell of the grid is assumed to contain a uniform magnetostatic charge density, determined via a discrete approximation to $\rho = -\nabla \cdot \mathbf{M}$.

To calculate the potential from the charge distribution in the particle, the Fourier transform of the charge distribution is multiplied by a kernel which is the Fourier transform of the potential due to a single cell with unit uniform charge. The inverse transform of this product yields the potential. In the final step, the in-plane magnetostatic field is calculated by a discrete approximation to the gradient of the potential.

The computational cost of this method for computing $\mathbf{H}^{\mathrm{D}}_{\mathbf{x,y}}$ includes two real FFT's, and two numerical differentiations for computation of $\rho = -\nabla\cdot\mathbf{M}$, and $\mathbf{H} = -\nabla\Phi$ per evaluation.

II. RESULTS AND DISCUSSION

For each value of d/l_{ex}, hysteresis loops were calculated using cell sizes ranging from $0.1d$ down to $0.02d$. Starting from from $H_x = H_y = H_z = -7.96 \times 10^{-2} M_s$ ($\mu_0 H_x =$ -100 mT, $M_s = 10^6$ A/m), the applied field was increased to zero in 10 steps. The field was then incremented in the [1,1,1] direction in steps of $\Delta H_x = \Delta H_y = \Delta H_z = 7.96 \times 10^{-4} M_s$.

As a function of d/l_{ex}, it is convenient to label the coercivity of the particle according to the instability that initiates the magnetization reversal: nonuniform rotation, end domain reversal, or vortex formation. Magnetization states associated with these processes are shown in Fig. 3.

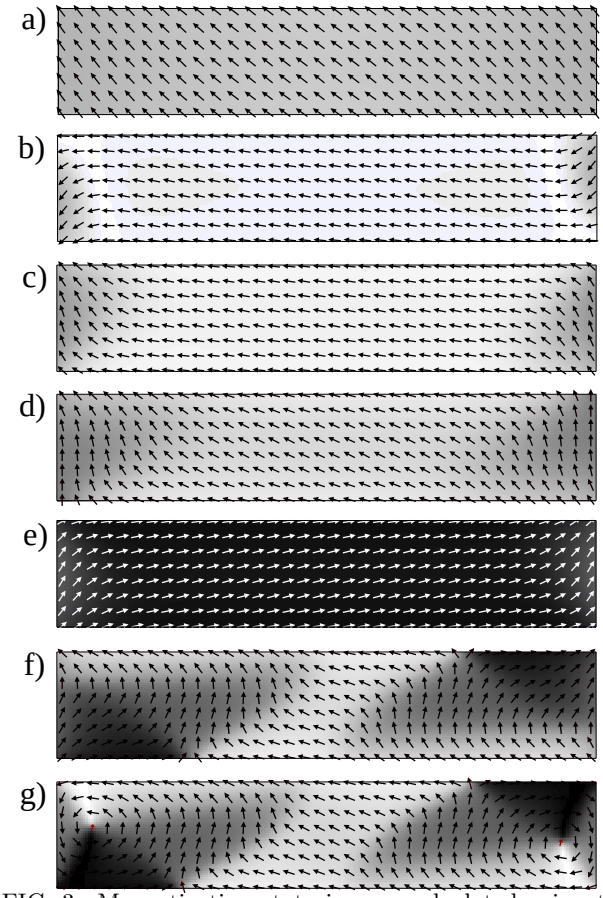

FIG. 3. Magnetization state images calculated using the constant magnetization method a) just before switching, d/l_{ex}= 3.0, and b)–e) for various fields at d/l_{ex}=17.8 including b) and c) the field steps just before and after end domain switching, and d) and e) the field steps just before and after magnetization reversal via end domain propagation. Transient states f) and g) were captured during end domain propagation and vortex propagation at d/l_{ex}= 31.6 and d/l_{ex}= 40, respectively. The grey scale displays M_x, with white for $M_x = -1.0$ and black for $M_x = 1.0$.

Nearly uniform rotation is the reversal mechanism for the smallest values of d/l_{ex}, $d/l_{\mathrm{ex}} <\approx 10$, where the remanent state is symmetric about the long axis of the sample. Magnetization reversal for these length scales is nearly uniform, (see Fig. 3a) but with magnetization near the ends tending to rotate more easily in the applied field than in the center of the strip. At $H <\approx H_c$, only a small component of the magnetization appears out of plane ($M_z/M_s < 0.05$), and the average $\mathbf{M}$ is nearly perpendicular to $\mathbf{H}$ ($M_{||}/M_s < 0.003$). Because M_z is small, this result can be compared with the Stoner-Wohlfarth model, which predicts that with the field applied at 45° to the particle axis, the magnetization lies perpendicular to the field at fields approaching coercivity.

For intermediate values of d/l_{ex}, $10 <\approx d/l_{\mathrm{ex}} <\approx 32$, the remanent state is asymmetric, with transverse end

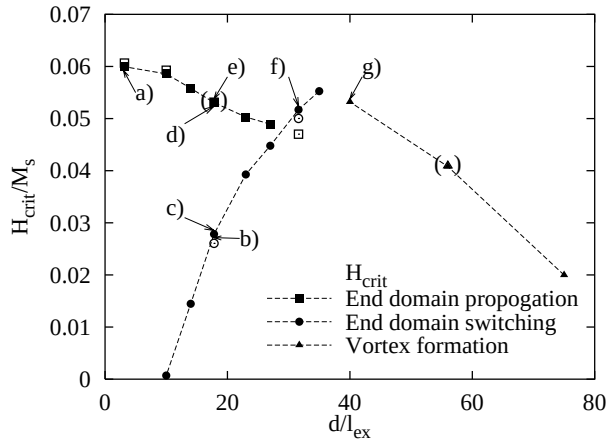

FIG. 4. Critical fields for μMAG standard problem #2 as a function of reduced particle width $d/l_{\rm ex}$. The symbol size is approximately equal to the uncertainty in H_c/M_s due to the field step size. Filled and open symbols are results obtained using the constant magnetization and constant charge methods, respectively. Superimposed data points are enclosed by parentheses. Labels a–g correspond to magnetization patterns displayed in Fig. 3

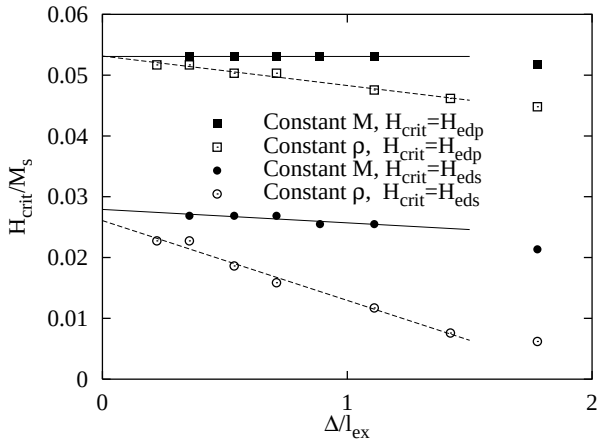

FIG. 5. Critical fields for μMAG standard problem #2 as a function of normalized cell size $\Delta/l_{\rm ex}$ with $d/l_{\rm ex}$=17.8. Squares indicate end domain propagation fields ($H_{\rm edp}$) and circles indicate end domain switching fields ($H_{\rm eds}$). Filled and open symbols are results obtained using the constant magnetization and constant charge methods, respectively.

domains formed in opposite corners of the sample at remanence (see Fig. 3b). As the field is increased in magnitude along the [1,1,1] direction, a critical field $H_{\rm eds}$ is reached for end domain switching where the magnetization in the end domain switches from the $-y$ direction to the $+y$ direction (see Figs. 3b,c). At the coercive field $H_{\rm edp}$ the end domains propagate inwards from the ends of the sample and annihilate. These traveling walls are very reminiscent of the static transverse head-to-head domain walls calculated previously for infinitely long thin magnetic strips[6].

For $29 <\approx d/l_{\rm ex} <\approx 35$, $H_{\rm eds}$ is greater than $H_{\rm edp}$. In this range, the end domains switch and propagate without an intermediate stable state.

For $d/l_{\rm ex} >\approx 35$, the end domains lose stability not by switching, but by nucleation of vortices on the long edges of the sample near the ends. These vortices then move across the ends of the sample as the magnetization reverses. The transient structure that appears after vortex formation bears a striking resemblance to a similar vortex end domain structure that has been observed in lithographically prepared structures[7]. It appears that the vortex end structures are formed at a field that exceeds their stability limit because in the same field step that produces the vortex end domains, the magnetization reverses by extension and collision of the end domains. We suspect that because the vortex end domains are spatially larger than the transverse end domains, there is not enough room for vortex head-to-head domain walls[6] of the type observed by Rürhig et al.[7] to be clearly separated from the ends.

It is interesting to note that the minimum energy head to head domain wall configuration in infinite strips has been reported[6] to change from transverse wall to vortex wall at $t \cdot d = 65 l_{ex}^2$, corresponding to $d/l_{\rm ex}$= 25.5 here, which is in the neighborhood of the transition from transverse end domain propagation to vortex formation reported above.

III. COMPARISON OF TECHNIQUES

The convergence properties of the constant magnetization and constant charge methods are illustrated in Fig. 5. The constant magnetization method is less sensitive to cell size, and converges with a more straightforward extrapolation to zero cell size than the constant charge method.

The magnetostatic computational methods described above share the approximations that the magnetostatic field is calculated only at a single location in each cell, and that for constant particle thickness, the cell aspect ratio changes with cell size. These two approximations are related in that when the cell aspect ratio is very different from 1.0, the field at the cell center may not be a good approximation to the field average, even for very small cell sizes.

The constant charge method carries a further approximation that the surface magnetostatic charges on the sample edges are represented by blocks of charge, rather than a true surface charge. As the cell size is reduced, the bulk edge charge distribution approximates a surface charge, but we suspect that changes in edge charge distribution with cell size may be responsible for the poorer convergence properties of this method. Edge charge corrections may be incorporated into this scheme at additional computational cost[3].

While the computational cost of the constant charge

method without edge correction is less than that of the constant magnetization method, the constant magnetization method appears to have superior convergence properties when edge and surface effects are important.

---

[1] The μMAG standard problems definitions are available at http://www.ctcms.nist.gov/~rdm/mumag.html.

[2] C.-C. Sher, *IEEE Trans. MAG*, **17**, 2401 (1981).

[3] K. Ramstöck, T. Leibl and A. Hubert, *J. Magn. Magn. Mater.* **135**, 97 (1994)

[4] D. V. Berkov, K. Ramstöck, and A. Hubert, *Phys. Stat. Sol. A*, **137**, 207 (1993).

[5] M. J. Donahue and R. D. McMichael, *Physica B,* **233**, 272 (1997).

[6] R. D. McMichael and M. J. Donahue, *IEEE Trans. MAG*, **33**, 4167, (1997).

[7] M. Rührig, B. Khamsepour, K. J. Kirk, J. N. Chapman, P. Aitchison, S. McVitie, and C. D. W. Wilkinson, *IEEE Trans. MAG*, **32**, 4452, (1996).